Available online at www.sciencedirect.com

SciVerse ScienceDirect

Journal of the European Ceramic Society 32 (2012) 589–602

www.elsevier.com/locate/jeurceramsoc

Original Article

An algorithm for the generation of silicon nitride structures

Johannes Wippler*, Thomas Böhlke

Chair for Continuum Mechanics, Institute of Engineering Mechanics, Karlsruhe Institute of Technology (KIT), Germany

Received 5 July 2011; received in revised form 21 September 2011; accepted 1 October 2011
Available online 27 October 2011

Abstract

Silicon nitride is used for demanding tasks due to its high stiffness, strength and, especially, its high fracture toughness. Examples include cutting tools, forming rolls and ball bearings. The microstructure is characterized by elongated β-Si_3N_4 grains of different size and shape, which lead to the increased fracture toughness. Consequently, the paper will present an algorithm for the generation of three-dimensional and periodic silicon nitride-like microstructures, which will be used for micromechanical finite element simulations. The structure generation algorithm enhances the sequential adsorption technique with growth of particles and steric hindrance, which are motivated by experimental results. Results of the structure generator, such as the pseudo-time evolution and its statistical geometric distributions are presented and compared to literature data. With the finite element simulations, using a periodic unit cell, a validation of the model with literature values for Young's modulus and Poisson's ratio was possible.

Keywords: C. Si_3N_4; C. Toughness and toughening; E. Structural applications; E. Cutting tools; Grain size and shape distribution

1. Introduction

Silicon nitride is a structural reinforced ceramic, which is used for high performance applications due to its fair compromise of stiffness, strength and toughness. This interesting property profile is related to different aspects of the material on the microlevel. Its strength and fracture toughness depends strongly on two features: The grain size-shape distribution and, furthermore, the properties of the grain boundary films are equally relevant for the effective mechanical material properties.

The observation of the structure–property relationship is a long-term field of research. Lange[1] was one of the first to the knowledge of the authors, who investigated a relation between fracture energy and the microstructure of hot-pressed silicon nitride. He reported results of double cantilever specimens, which clearly indicate a correlation between the measured fracture energy and the detected elongated grains in β-rich silicon nitride compositions. It was observed that the samples, which dissipated the most fracture energy had a significantly increased specific surface with deep holes from pulled out grains of high aspect ratio.

Ohji et al.[2] and Becher et al.[3] found that especially a bimodal distribution of grain sizes with an isotropic distribution of the grain axes is increasing the fracture toughness, whereas large and elongated grains can act as bridges between the crack surfaces, such that cracks have to propagate under circumventing of the grains.

Different ways of achieving such microstructures have been examined. An example is given in Peillon,[4] where it was found that longer sintering times lead to a considerable improvement of the fracture toughness than seeding with big β-grains, since seeding can have unfavorable effects on the densification of the material. With increased seeding times and, thereby, longer periods of natural grain growth, fracture toughness could be improved by up to 30% with respect to the reference material.

In Sun et al.,[5] the influence of yttria and alumina additives have been examined with the result that a high Y:Al ratio is increasing the fracture resistance due to large and elongated grains with a relatively low debonding stress, which supports crack path deviation.

Different approaches to the simulation of silicon nitride microstructures have been documented. An important contribution is the implementation of the anisotropic Ostwald ripening for faceted crystals by Kitayama et al., [6] the α- to β-transition[7]

---

* Corresponding author. Tel.: +49 721 608 48852; fax: +49 721 44187.
E-mail addresses: johannes.wippler@kit.edu (J. Wippler), thomas.boehlke@kit.edu (T. Böhlke).

0955-2219/$ – see front matter © 2011 Elsevier Ltd. All rights reserved.
doi:10.1016/j.jeurceramsoc.2011.10.001

Nomenclature

Scalar variables

A	aspect ratio
B	grain thickness
c	grain volume fraction
$C^{\mathcal{G}}_{\alpha\beta}$	elastic stiffness constants of the grains
d	Euclidean distance
E	Young's modulus
G	shear modulus
$k_{B/L}$	grain growth velocity constant in basal/axial direction
L	grain length
ℓ	norm symbol for corresponding norms (p/max)
K	bulk modulus
ν	Poisson's ratio
r	random number
t	pseudo-time
V	volume
w	edge length of the unit cell
φ	azimuthal angle
ϑ	polar angle
ω	rotation angle

Sets

$\mathcal{D}$	set of grain dimensions
$\Delta\mathcal{D}$	grain dimension variation
$\mathcal{E}$	prism edges
$\mathcal{V}$	prism vertices
$\mathcal{F}$	prism faces
$\mathcal{L}$	contact indications
$\mathcal{P}$	projections

Vectors and tensors

$\boldsymbol{B}_\alpha$	second order basis tenors ($\alpha = 1 \ldots 6$)
$\mathbb{C}$	elastic stiffness tensor
$\boldsymbol{d}$	unit normal vector on unit sphere
$\boldsymbol{e}_i$	Cartesian unit vector ($i = 1 \ldots 3$)
$\boldsymbol{\varepsilon}$	infinitesimal strain tensor
ϵ	Levi–Civita symbol
$\boldsymbol{m}_i$	prism edge vectors ($i = 1 \ldots 6$)
$\boldsymbol{n}_i$	normal vector on the grains' prism planes ($i = 1 \ldots 8$)
$\boldsymbol{p}$	point
$\boldsymbol{Q}$	orientation tensor
$\boldsymbol{s}$	shift vector for grain origin translation
$\boldsymbol{\sigma}$	Cauchy stress tensor
$\boldsymbol{x}$	location

Sub- and superscripts

0	initial
acc	accumulated
$\mathcal{G}$	grain
ga	growing around
int	intersection
m	mean intersection point
$\mathcal{M}$	matrix
o	overlap
p	periodic copy
pen	penalty

and the shape evolution of a single grain in Ref.[8] The most important results in the light of the recent work are distributions of grain lengths, widths and aspect ratios, which are in good agreement with experimental observations and with the results obtained by the presented method for the synthetic generation of silicon nitride-like structures. However, it has to be mentioned that the method was not meant to resolve the microstructure itself by the algorithm.

The effective mechanical properties of a polycrystalline material can be calculated from information on the microlevel. A classical approach is the usage of a unit cell that is assumed to represent the geometrical and the material information of the considered bulk material. Given the statistical "representativity", the unit cell is often called a representative volume element (RVE). The best way for creating such a unit cell is the direct usage of experimental data. Borbély et al.[9] have applied microtomographic observations on particle-reinforced metal-matrix composites (aluminum as matrix with 20% alumina particles as reinforcement) for the construction of finite element meshes.

In case of silicon nitride, this approach is not feasible due to the extremely challenging preparation techniques. Therefore, it is technically not possible, to use a sequence of scanning electron microscope (SEM) images for the in-depth information on the silicon nitride geometry. The required slice thickness lies in the sub-micrometer domain due to the given grain sizes and cannot be delivered by recent preparation techniques. The application of image-giving techniques like magnetic resonance tomography (MRT) or micro computer tomography (Micro-CT) is impossible due to the low phase contrast and the very small intrinsic dimensions, which are significantly beneath the accessible resolution. First investigations of image stack acquisition by a combination of electron backscatter diffraction (EBSD) for the image acquisition and focused ion beam sections (FIB) for the in-depth segmentation have been undertaken. However, they are much too expensive for an efficient geometry reconstruction.

Thus, a different way had to be chosen, which was inspired by the sequential adsorption technique. It allows for an algorithmic creation of a structure, which is similar to experimental observations. Louis and Gokhale [10] created a synthetic microstructure of a polymer matrix composite with spherical inclusions of constant size. The geometry was used to obtain a self-consistent model for the electrical conductivity. Tschopp et al.[11] used two-dimensional distributions of ellipses with different aspect ratios, which have been assembled into representative area elements for an examination of image analysis methods.

The presented algorithm for silicon nitride-like structure combines the sequential adsorption technique, see, e.g., Cooper,[12] with particle growth and subsequent steric hindrance and is based on experimental observations on the grain growth processes. It has to be emphasized that the algorithm does not consider any chemical or thermodynamical relations.

OUTLINE: The paper will give a detailed introduction into the microstructure generation algorithm with the applied geometric quantities and the corresponding randomization of the geometry. The algorithmic consideration of the steric hindrance, also known as pinning, is presented with its geometrical a logical implementation. The section ends with a short overview on the periodization of the geometry.

Results of the implemented structural model will be shown for periodic microstructures containing 27 × 1050 grains. First, the pseudo-time evolution, the grain volume fraction and the aspect ratio will be presented. Afterwards, the distributions of grain length and aspect ratio from experimental observations of Fünfschilling et al.[13] will be compared to the results of the generated microstructure.

Finally, the structure generator is used for the generation of finite element models. In this line, simulations on periodic unit cells with 232 grains have been carried out, in order to determine the effective elastic stiffness of silicon nitride, Wippler et al.[14] The discretized finite element geometry resulting from the mesh generation with Simpleware[15] will be discussed. The elastic material models, i.e., transverse-isotropic elasticity for the grains and isotropic elasticity for the glassy phase will be introduced. A short summary on the projected periodic boundary conditions applied, the elastic homogenization technique and its results will follow. A discussion in the light of further applications and several conclusions complete the paper.

Notation. A direct tensor notation is preferred throughout the text. Vectors and 2nd-order tensors are denoted by lowercase and uppercase bold letters, e.g., $\boldsymbol{a}$ and $\boldsymbol{A}$, respectively. A linear mapping of 2nd-order tensors by a 4th-order tensor $\mathbb{C}$ is written as $\boldsymbol{A} = \mathbb{C}[\boldsymbol{B}]$. The scalar product and the dyadic product between vectors and tensors are denoted by $\boldsymbol{a} \cdot \boldsymbol{b}$ and $\boldsymbol{a} \otimes \boldsymbol{b}$, respectively. The brackets $\langle \cdot \rangle$, e.g., $\langle \boldsymbol{\sigma} \rangle$, indicate ensemble averaging, which can be identified with volume averages in the infinite volume limit for ergodic media. The effective quantities are denoted by a bar, e.g., $\overline{\mathbb{C}}$. The tensor $\boldsymbol{I}$ is the identity on vectors. The identity on symmetric 2nd-order tensors represents $\mathbb{I}^S$. All tensorial quantities are embedded in the three-dimensional Euclidean space $\mathbb{R}^3$.

2. Microstructure generation

2.1. Overview

The main idea of the structural model is based on the fact that the silicon nitride-like structure is arising from statistical seeded locations and orientations of hexagonal prisms, which will be called "grains" in the context of this work. The grains are seeded in an adjustable number of steps and are thought to be growing isotropically until steric hindrance arises. The cases of the pinning need a specific consideration, which will be given later on. After the calculation of the "exact" structure, the determination of the voxel structure, which is necessary for the finite element discretization, allows for certain smaller refinements like the angularity of the grains and the matrix volume fraction of the structure.

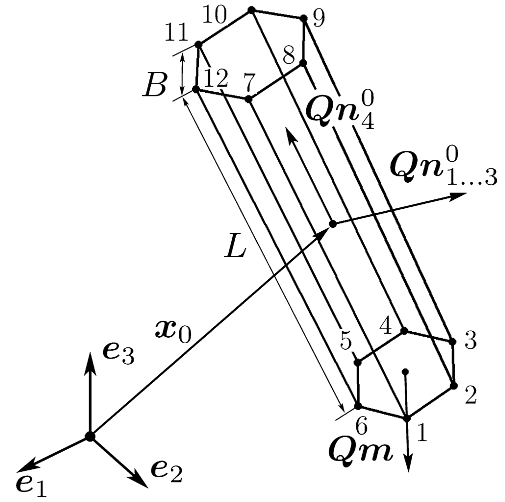

Fig. 1. Grain lattice model in a general configuration: hexagonal prism with coordinate system, origin, prism normal, edge vectors and dimensions; vertice numbers correspond with edge set $\mathcal{E}$.

2.2. Geometric quantities

On the one hand, grains, i.e., hexagonal prisms, can be regarded as sets of vertices, edges and planes. An equivalent representation is provided by the norm concept, such that grain-like contours can be described by the norm $\ell^{\max} \leq 1$, which will be introduced in Eq. (6).

Both concepts use the grain origin $\boldsymbol{x}_0$, the unit normal vectors of the hexagonal prism and its dimensions B and L for the breadth and length, respectively (Fig. 1). The orthogonal orientation tensor $\boldsymbol{Q}$ is given by the angle-axis representation $\boldsymbol{Q} = \boldsymbol{Q}(\boldsymbol{d},\omega) = \boldsymbol{d} \otimes \boldsymbol{d} + (\boldsymbol{I} - \boldsymbol{d} \otimes \boldsymbol{d}) \cos(\omega) - \epsilon[\boldsymbol{d}] \sin(\omega)$ with the rotation angle ω. The rotation axis $\boldsymbol{d}$ is given by the normal vector on the unit sphere with $\boldsymbol{d} = \boldsymbol{d}(\vartheta, \varphi) = \sin(\vartheta)\cos(\varphi)\,\boldsymbol{e}_1 + \sin(\vartheta)\sin(\varphi)\,\boldsymbol{e}_2 + \cos(\vartheta)\boldsymbol{e}_3$, where $\boldsymbol{I} = \boldsymbol{e}_i \otimes \boldsymbol{e}_i$ is the identity tensor and $\epsilon = \boldsymbol{e}_i \cdot (\boldsymbol{e}_j \times \boldsymbol{e}_k)\,\boldsymbol{e}_i \otimes \boldsymbol{e}_j \otimes \boldsymbol{e}_k$ is the Levi–Civita permutation tensor. The set of normal vectors on the faces in the initial configuration is given by $\boldsymbol{n}_1^0 = \boldsymbol{e}_1, \boldsymbol{n}_2^0 = 1/2\ (\boldsymbol{e}_1 + \sqrt{3}\boldsymbol{e}_2), \boldsymbol{n}_3^0 = 1/2\ (-\boldsymbol{e}_1 + \sqrt{3}\boldsymbol{e}_2)$, and $\boldsymbol{n}_4^0 = \boldsymbol{e}_3$. The first three vectors represent the three different orientations of the positive prism planes. The fourth vector describes the direction of the upper basal plane. Changing the signs of the vectors provides the opposing planes. The set $\mathcal{D} = 1/2\ \{\sqrt{3}B, \sqrt{3}B, \sqrt{3}B, L\}$ assembles the distances of the prism planes to the grain origin $\boldsymbol{x}_0$ with the dimensionless breath B and length L.

The 12 vertices of the grains are given by the set

$$\mathcal{V} = \left\{ \boldsymbol{v} | \boldsymbol{v} = \boldsymbol{x}_0 + B\,\boldsymbol{m}_i \pm \frac{1}{2} H\,\boldsymbol{n}_4,\ \ i = 1 \ldots 6 \right\}, \tag{1}$$

with the edge vectors $\boldsymbol{m}_i = 1/2\ (\boldsymbol{n}^{\mathcal{V}}_{i \bmod 6+1} + \boldsymbol{n}^{\mathcal{V}}_i),\ \ i = 1 \ldots 6$, the normal vectors on the prism planes in positive and negative directions $\boldsymbol{n}^{\mathcal{V}} = \{\boldsymbol{Q}\boldsymbol{n}_i^0, -\boldsymbol{Q}\boldsymbol{n}_i^0\}$ and $i = 1\ldots3$ and the axial vector $\boldsymbol{n}_4 = \boldsymbol{Q}\boldsymbol{n}_4^0$.

The set of 18 edges consists of three subsets. The set of six prism edges $\mathcal{E}^{\mathrm{p}}$ and two sets of each six basal edges $\mathcal{E}_1^{\mathrm{b}}$ and $\mathcal{E}_2^{\mathrm{b}}$ with

$$\begin{aligned}
\mathcal{E}^{\mathrm{p}} &= \{\boldsymbol{x} \mid \boldsymbol{x} = \boldsymbol{v}_i + s(\boldsymbol{v}_{i+6} - \boldsymbol{v}_i)\}\\
\mathcal{E}_1^{\mathrm{b}} &= \{\boldsymbol{x} \mid \boldsymbol{x} = \boldsymbol{v}_i + s(\boldsymbol{v}_{i \bmod 6+1} - \boldsymbol{v}_i)\} \qquad (2)\\
\mathcal{E}_2^{\mathrm{b}} &= \{\boldsymbol{x} \mid \boldsymbol{x} = \boldsymbol{v}_{i+6} + s(\boldsymbol{v}_{i \bmod 6+7} - \boldsymbol{v}_{i+6})\},
\end{aligned}$$

with $s = [0, 1]$ and $i = 1\ldots6$. Thus the general set of edges is $\mathcal{E} = \mathcal{E}^{\mathrm{p}} \cup \mathcal{E}_1^{\mathrm{b}} \cup \mathcal{E}_2^{\mathrm{b}}$.

The eight faces $\mathcal{F}$ consist of six prism faces and two basal faces with the normal form

$$\mathcal{F} = \{\boldsymbol{x} | \boldsymbol{x} \cdot \boldsymbol{n}_i^{\mathcal{F}} - \boldsymbol{n}_i^{\mathcal{F}} \cdot (\boldsymbol{x}_0 + \mathcal{D}_i \boldsymbol{n}_i^{\mathcal{F}}) = 0, \quad i = 1\ldots8\}. \qquad (3)$$

The outward normal vectors on the prism faces are $\boldsymbol{n}_i^{\mathcal{F}} = \{\boldsymbol{Q}\boldsymbol{n}_i^0, -\boldsymbol{Q}\boldsymbol{n}_i^0\}$ with $i = 1\ldots4$.

The ℓ^p-norm is a generalization of the Euclidean norm ($p = 2$) with respect to both the exponent p and the used base vectors $\boldsymbol{n}_i$, $i = 1\ldots4$. The formal representation of the grains is given by the ℓ^p-norm on the projections $\mathcal{P}$ of the difference of a certain point $\boldsymbol{x}$ in space to the origin of the grain $\boldsymbol{x}_0$ on the oriented normal planes with normal vector $\boldsymbol{n}_i$ and the length scale $\mathcal{D}_i$

$$\mathcal{P}_i(\boldsymbol{x}) = \frac{1}{\mathcal{D}_i}\, \boldsymbol{Q}\boldsymbol{n}_i^0 \cdot (\boldsymbol{x} - \boldsymbol{x}_0), \quad i = 1\ldots4. \qquad (4)$$

Hence, the norm then can be written

$$\ell^p(\boldsymbol{x}) = \sqrt[p]{\sum_{i=1}^{4} |\mathcal{P}_i(\boldsymbol{x})|^p}. \qquad (5)$$

As limiting case $p \to \infty$, the ℓ^p-norm transforms into the maximum norm

$$\ell^{\max}(\boldsymbol{x}) = \max\{|\mathcal{P}_i(\boldsymbol{x})|, \quad i = 1\ldots4\}. \qquad (6)$$

The anisotropy can be obtained by the choice of the normal vectors $\boldsymbol{n}$ and the dimensions $\mathcal{D}$. Fig. 2 shows several cases. The transition from the Euclidean norm to an angular form and with high aspect ratios can be clearly observed.

2.3. Randomization

For a statistical structure generation, a homogeneous statistical distribution of locations, orientations and growth parameters are the precondition, which can deliver an isotropic orientation distribution, if enough grains are in the statistical ensemble. The origin of a grain $\boldsymbol{x}_0$ depends on three random numbers $r_{1\ldots3}$ in the range of 0 and 1. The vectors are scaled by the edge length w of the cube of consideration, such that the grain origin is $\boldsymbol{x}_0 = w(r_1\,\boldsymbol{e}_1 + r_2\,\boldsymbol{e}_2 + r_3\,\boldsymbol{e}_3)$. Here, it is useful to avoid points, which are too close to each other to allow for a noteworthy growth. The penalty distance of a set of points is determined by the notion of an assumed mean density $\langle V^{\mathcal{G}}\rangle = w^3/n^{\mathcal{G}}$, with the intended number of grains in the unit cell $n^{\mathcal{G}}$. Thus, the mean distance is $\langle d^{\mathcal{G}}\rangle = \sqrt[3]{\langle V^{\mathcal{G}}\rangle}$, and the penalty distance is $d^{\mathrm{pen}} = k^{\mathrm{pen}}\langle d^{\mathcal{G}}\rangle$, with the penalty factor $0 < k^{\mathrm{pen}} < 1$. A new grain origin $\boldsymbol{x}_0^2$, which is seeded next to an already existing grain origin $\boldsymbol{x}_0^1$ is not used, if $\|\boldsymbol{x}_0^1 - \boldsymbol{x}_0^2\| < d^{\mathrm{pen}}$. Feasible values for the penalty factor k^{pen} are between 1/4 and 1/2. Fig. 3 shows four examples in two dimensions. The impact of the penalty factor is significant. With increasing penalty factor, the mean distance between the objects increases, due to the enforced distance around them. This means for the sequential adsorption that undesirable grain clusters are avoided. These clusters would end in an early-stage growth hinderance, which delivers structures with low aspect ratios and, therefore, unrealistic stereologic properties.

In case of reseeding, all new grain origins have to be checked for being inside an already existing grain. Here, the penalty distance $\Delta\mathcal{D}^{\mathrm{pen}}$ is used in the projection

$$\mathcal{P}_i^{\mathrm{pen}} = \frac{\boldsymbol{n}_i^1 \cdot (\boldsymbol{x}_0^2 - \boldsymbol{x}_0^1)}{\mathcal{D}_i^1 + \Delta\mathcal{D}^{\mathrm{pen}}}, \quad i = 1\ldots4 \Rightarrow \ell_{12}^{\mathrm{pen}} = \max\{|\mathcal{P}_i^{\mathrm{pen}}|, \quad i = 1\ldots4\}. \qquad (7)$$

Reasonable values for $\Delta\mathcal{D}^{\mathrm{pen}}$ are in the range of 1…5% of the edge length w.

The growth for the prismatic (breadth B) and basal direction (length L) relations are given by

$$k_B = (1 + c_B(1 - 2r_4))\,k_B^0, \qquad \Delta B = k_B\,\Delta t, \quad B = k_B\,t, \qquad (8)$$

$$k_L = (1 + c_L(1 - 2r_5))\,k_L^0, \qquad \Delta L = k_L\,\Delta t, \quad L = k_L\,t, \qquad (9)$$

such that the growth velocities are scattering around $k_{B/L}(1 \pm c_{B/L})$.

The homogeneous distribution of the random numbers on the unit sphere requires a remapping of the pseudo-random numbers $r_{6\ldots8}$ due to the curvature of the sphere. According to Shoemake,[16] the relations $\vartheta = \arccos(1 - 2r_6)$, $\varphi = 2\pi\, r_7$ and $\omega = \sin(\omega) - \pi\, r_8$ are used to achieve a homogeneous orientation distribution on the unit sphere $SO(3)$. The rotation angle ω has to be calculated numerically.

Hence, the whole system is determined by $8\,n^{\mathcal{G}}$ random numbers. These pseudo-random numbers are provided by the generator "sunif".[17]

2.4. Steric hinderance

2.4.1. Experimental observations

The development of the silicon nitride structure is strongly influenced by the steric impingement of the grains. Krämer et al.[18] have made three important observations on pinning (Fig. 4):

Observation 1: "The growth of a basal plane of a β-grain is stopped, when it hits a prism plane of another one as shown by arrow 1."

Observation 2: "If the thickness of a β-grain is comparatively large, its basal plane grows around a prism plane of a

Fig. 2. Contour of the anisotropic norm $\ell^p(\boldsymbol{x}) = 1$ with increasing exponents $p = \{2, 5, 10, 20\}$ and aspect ratios: the angularity of the grain models increases with increasing values for the exponent p. Natural shapes are obtained by high values, e.g., $p = 10 \ldots 20$ and $L/B = 3 \ldots 10$. The left contour is an ellipse, i.e., an Euclidean norm for $p = L/B = 2$.

neighbouring grain (arrow 2) through the 'free space' of liquid pockets and can include smaller grains."

Observation 3: "Edges and corners of prism planes are frequently rounded in case of edge-on-plane contact with other grains (arrow 3)."

2.4.2. *Implementation of Krämer's first observation: growth and pinning*

The implementation of a conclusive growth-after-pinning behavior is one of the main achievements of this work. The numerical implementation of the first observation is done by the

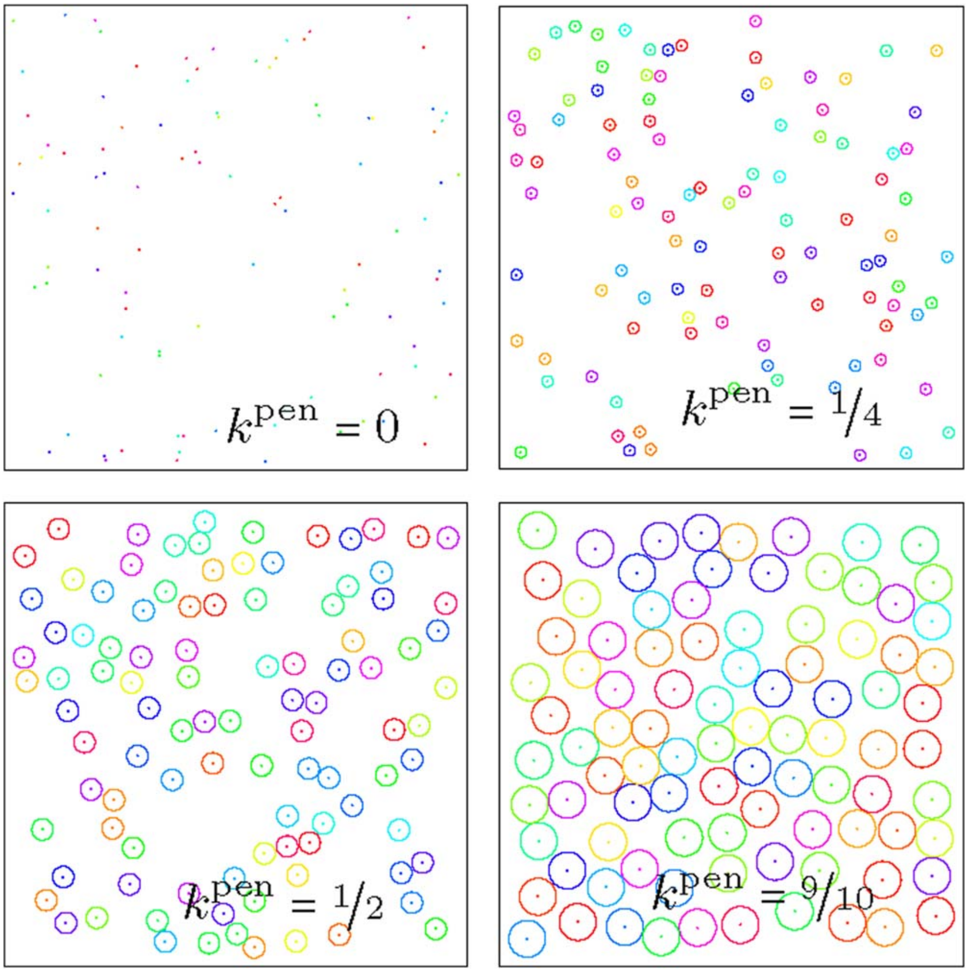

Fig. 3. Influence of the penalty distance on the sequential adsorption technique demonstrated on random seeded points in two dimensions with penalty factor $k^{\text{pen}} = \{0, 1/4, 1/2, 9/10\}$. The magnitude of the penalty is indicated by the circles around the points. The higher the penalty factor, the larger the mean distance between neighboring objects.

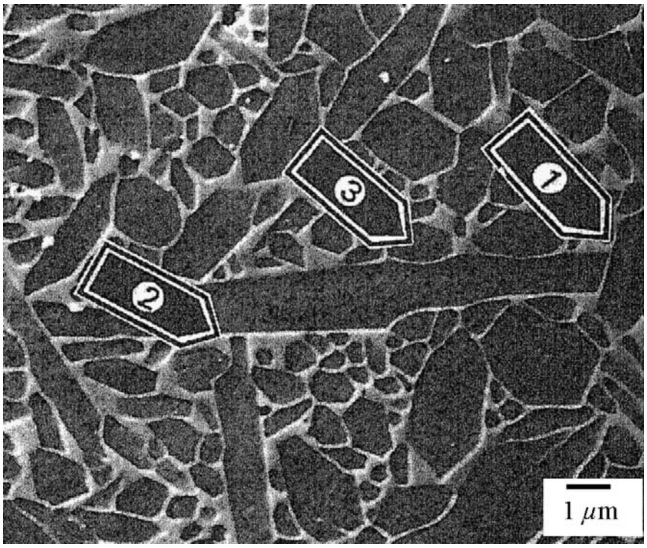

Fig. 4. Three observations on grain pinning of Krämer et al.[18] Arrow 1 shows the case, when "a basal plane of a β-grain . . . hits a prism plane of another one . . ."; arrow 2 displays that, when "the thickness of a β-grain is comparatively large, its basal plane grows around a prism plane of a neighbouring grain through the 'free space' of liquid pockets and can include smaller grains"; arrow 3 visualizes the rounding of grain boundaries "in case of edge-on-plane contact with other grains".

consideration of an intersection of the 18 edges $\mathcal{E}_\mathrm{s}$ of a smaller grain (s) with the eight faces of the bigger grain (b), $\mathcal{F}_\mathrm{b}$. Here, the intersection points $\boldsymbol{p}^\mathrm{int}$ are determined by $\mathcal{E}_\mathrm{s} \cap \mathcal{F}_\mathrm{b}$. The line segment for a certain edge is given by Eq. (2), such that $\boldsymbol{x}_\mathrm{s}(s) \cdot \boldsymbol{n}_\mathrm{b} = d_\mathrm{b}$ is a projection of a point on an edge onto a face with the normal $\boldsymbol{n}_\mathrm{b}$ and the distance of the face to the origin of the coordinate system $d_\mathrm{b} = (\boldsymbol{x}_{0,\mathrm{b}} + \mathcal{D}_\mathrm{b}\boldsymbol{n}_\mathrm{b}) \cdot \boldsymbol{n}_\mathrm{b}$. The line segment parameter s is determined by $s = (d_\mathrm{b} - \boldsymbol{v}_\mathrm{s}^1 \cdot \boldsymbol{n}_\mathrm{b})/((\boldsymbol{v}_\mathrm{s}^2 - \boldsymbol{v}_\mathrm{s}^1) \cdot \boldsymbol{n}_\mathrm{b})$ and has to be in its co-domain [0, 1] that $\boldsymbol{x}^{\mathcal{V}_i^1}$ is a candidate for a valid intersection point $\boldsymbol{p}^\mathrm{int}$. If this necessary condition is fulfilled, a second check has to be done: the validity of $\boldsymbol{x}^{\mathcal{V}_i^1}$ can be seen if $\ell_\mathrm{b}^\mathrm{max}(\boldsymbol{x}_\mathrm{s}(s)) \leq 1$. If the sufficient condition is met as well, $\boldsymbol{p}^\mathrm{int} := \boldsymbol{x}_\mathrm{s}(s)$. In general, there will be at least three intersection points for a finite penetration of two grains. For the sake of simplicity, the mean value of these intersection points $\boldsymbol{p}^\mathrm{m}$ is used for the determination of the pinning case and the post-pinning growth. After the determination of the mean intersection point $\boldsymbol{p}^\mathrm{m}$, the interaction case between the grains is determined from the projections $\mathcal{P}^*$ by

$$\mathcal{P}_i^*(\boldsymbol{p}^\mathrm{m}) = \frac{\boldsymbol{n}_i \cdot s(\boldsymbol{p}^\mathrm{m} - \boldsymbol{x}_0)}{\mathcal{D}_i - \Delta\mathcal{D}}, \quad i = 1 \ldots 4. \tag{10}$$

The difference $\Delta\mathcal{D}$ has to be chosen, because the mean-intersection points lay in general inside the grains due to the finite growth velocities in discrete pseudo-time increments. The mean length increment $k_L(1 + c_L)\Delta t$ is a feasible choice. For the determination of the pinning-cases, $\mathcal{P}_i^*(\boldsymbol{p}^\mathrm{m}) = \pm 1$, $i = 1 \ldots 4$ is evaluated. The contact with more than one grain and the related post-pinning growth can be described by averaging over the mean intersection points from all contacts, if both or none of the basal planes are involved in contact. For the remaining cases, a point in the region of the basal edges has to be used.

For the sake of brevity, the relevant information of the projections $\mathcal{P}^*$ is condensed into a boolean list $\mathcal{L}$ of length 8. The default value is $\mathcal{L}_i = \mathit{false}, \ \ i = 1 \ldots 8$ and means no contact. In case of contact, $\mathcal{L}$ is set. The indices $1 \ldots 3$ and $5 \ldots 7$ designate the opposing prism faces. The indices 4 and 8 are for the upper and lower basal face.

$$\left.\begin{aligned} \mathcal{L}_i &= \mathit{true} \ \text{ if } \ \mathcal{P}_i^* = 1, \\ \mathcal{L}_{i+4} &= \mathit{true} \ \text{ if } \ \mathcal{P}_i^* = -1 \end{aligned}\right. \quad \text{and} \quad i = 1 \ldots 4. \tag{11}$$

The following case consideration is used to describe the post-contact growth in the structure generator. It is a simple implementation of the observation 1 of Ref.[18] For cases, which are not directly included, reasonable approaches have been chosen, which avoid uncontrolled grain interpenetration and allow for high volume fractions and aspect ratios.

Case 1. None of the prism planes are in contact $\left(\wedge_{i=1}^3(\neg\mathcal{L}_i \wedge \neg\mathcal{L}_{i+4})\right)$:

1.1: No contact $(\neg\mathcal{L}_4 \wedge \neg\mathcal{L}_8)$: default case, free growth in all directions.
1.2: One of the basal planes is in contact $((\mathcal{L}_4 \vee \mathcal{L}_8) \wedge \neg(\mathcal{L}_4 \wedge \mathcal{L}_8))$: free growth is allowed in all prism directions and axial growth is only possible in opposite contact direction. The grain origin is shifted by $\Delta\boldsymbol{x} = \mp 1/2\, \Delta L\, \boldsymbol{n}_4$.
1.3: Both basal planes are in contact $(\mathcal{L}_4 \wedge \mathcal{L}_8)$. Grains can grow in all prism directions, however, no axial growth is allowed, which implies no shift of the grain origin.

Case 2. No opposing prism planes are in contact $(\vee_{i=1}^3[(\neg\mathcal{L}_i \wedge \mathcal{L}_{i+4}) \vee (\mathcal{L}_i \wedge \neg\mathcal{L}_{i+4})])$:

2.1: No basal faces are in contact $(\neg\mathcal{L}_4 \wedge \neg\mathcal{L}_8)$: grains can grow further in both dimensions with half the velocity for the radial direction. The origin of the grain is shifted by $\Delta\boldsymbol{x}_0 = 1/2\, \Delta B \boldsymbol{s}$ with the normalized shift vector $\boldsymbol{s}$, which is determined by a projection of the difference vector on the mid plane in axial direction $\boldsymbol{s} = (\boldsymbol{I} - \boldsymbol{n}_4 \otimes \boldsymbol{n}_4)(\boldsymbol{x}_0 - \boldsymbol{p}^\mathrm{m})/\| \boldsymbol{x}_0 - \boldsymbol{p}^\mathrm{m} \|$.
2.2: One basal face is in contact $((\mathcal{L}_4 \vee \mathcal{L}_8) \wedge \neg(\mathcal{L}_4 \wedge \mathcal{L}_8))$: further growth is possible for both dimensions with half the velocity. The origin of the grain is shifted by $\Delta\boldsymbol{x}_0 = 1/2\sqrt{\Delta H^2 + 3\,\Delta B^2}\,\boldsymbol{s}$ with the direction from the basal edge to the origin of the grain $\boldsymbol{s} = (\boldsymbol{x}_0 - \boldsymbol{p}^\mathrm{m})/\| \boldsymbol{x}_0 - \boldsymbol{p}^\mathrm{m} \|$.
2.3: Both basal faces are in contact $(\mathcal{L}_4 \wedge \mathcal{L}_8)$: Only thickness can grow further. The origin of the grain is shifted as described for case 2.1.

Case 3. Opposing prism planes are in contact $\left(\vee_{i=1}^3(\mathcal{L}_i \wedge \mathcal{L}_{i+4})\right)$:

3.1: No basal faces in contact $(\neg\mathcal{L}_4 \wedge \neg\mathcal{L}_8)$: grain grows further only in axial direction with no shift of the grain origin.
3.2: One basal face in contact $((\mathcal{L}_4 \vee \mathcal{L}_8) \wedge \neg(\mathcal{L}_4 \wedge \mathcal{L}_8))$: further axial growth is allowed only in opposite axial

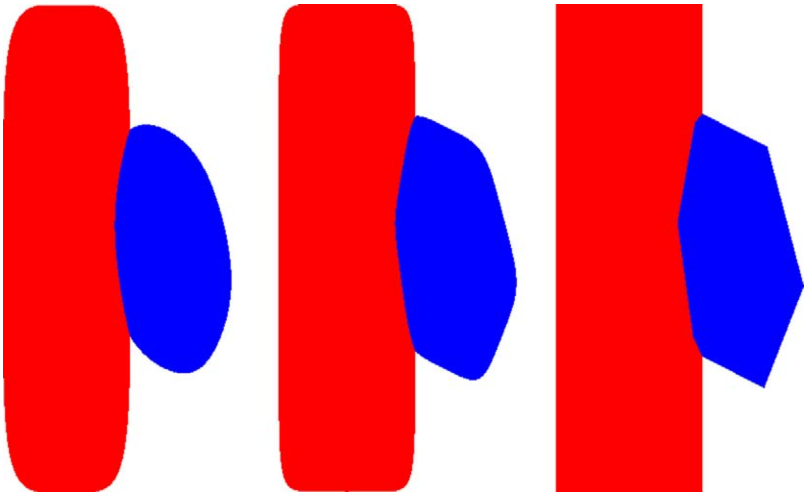

Fig. 5. Demonstration of the implementation of observation 3[18]: overlapping of grains for a fixed overlapping distance $\Delta\mathcal{D}^{\mathrm{o}} = B/2$ and increasing norm exponents $p = \{5, 10, \infty\}$ (from left to right). The angularity of the overlapping zone increases with the norm exponent. Naturally rounded overlapping and grain shapes can be obtained by a norm exponent of $p = 10$.

direction with half velocity with an origin shift as described for case 1.2.

3.3: Both basal faces in contact ($\mathcal{L}_4 \wedge \mathcal{L}_8$): Complete stop of growth.

2.4.3. Implementation of Krämer's second observation: growing around

The second observation of Krämer et al.[18] is implemented by the consideration of the axis distance and the thickness of two grains 1 and 2. The distance between to non-parallel lines is given by $d_{12} = \min\{\|s_1 \boldsymbol{n}_4^1 - s_2 \boldsymbol{n}_4^2 - \boldsymbol{r}_{12}\|\}$ with $\boldsymbol{n}_4^1 = \boldsymbol{Q}^1 \boldsymbol{n}_4$, $\boldsymbol{n}_4^2 = \boldsymbol{Q}^2 \boldsymbol{n}_4$ and $\boldsymbol{r}_{12} = \boldsymbol{x}_0^2 - \boldsymbol{x}_0^1$. The perpendicularity conditions $(s_1 \boldsymbol{n}_4^1 - s_2 \boldsymbol{n}_4^2 - \boldsymbol{r}_{12}) \cdot \boldsymbol{n}_4^1 = 0$ and $(s_1 \boldsymbol{n}_4^1 - s_2 \boldsymbol{n}_4^2 - \boldsymbol{r}_{12}) \cdot \boldsymbol{n}_4^2 = 0$, with $\boldsymbol{r}_{12} = \boldsymbol{x}_0^2 - \boldsymbol{x}_0^1$ deliver the linear system

$$\begin{bmatrix} s_1 \\ s_2 \end{bmatrix} = \frac{1}{1 - (\boldsymbol{n}_4^1 \cdot \boldsymbol{n}_4^2)^2} \begin{bmatrix} 1 & -\boldsymbol{n}_4^1 \cdot \boldsymbol{n}_4^2 \\ \boldsymbol{n}_4^1 \cdot \boldsymbol{n}_4^2 & -1 \end{bmatrix} \begin{bmatrix} \boldsymbol{r}_{12} \cdot \boldsymbol{n}_4^1 \\ \boldsymbol{r}_{12} \cdot \boldsymbol{n}_4^2 \end{bmatrix}. \tag{12}$$

This approach is not feasible for the special case of parallel lines. So the projection of the vector $\boldsymbol{r}_{12}$ on the perpendicular vectors is used. Then the distance is $d_{12} = \|(\boldsymbol{I} - \boldsymbol{n}_4^1 \otimes \boldsymbol{n}_4^1)\boldsymbol{r}_{12}\| = \sqrt{\boldsymbol{r}_{12} \cdot \boldsymbol{r}_{12} - (\boldsymbol{r}_{12} \cdot \boldsymbol{n}_4^1)^2}$. So the condition for "growing around" is $d_{12} > k^{\mathrm{ga}}(B_1 + B_2)$ with $0 < k^{\mathrm{ga}} < 1$ as allowed ratio of interpenetration. If this condition is fulfilled, there will be no further examination in the recent time step.

2.4.4. Implementation of Krämer's third observation: grain overlapping and rounding of grain interfaces

Krämer's[18] third observation is implemented in the context of the voxel discretization, which is used as an input for the finite element mesh generation. Here, a certain overlap of grains is reached by an offset value $\Delta\mathcal{D}^{\mathrm{o}}$ to the exact dimension $\mathcal{D}$ similarly to the offset, which allows for the usage of the projection information. The ℓ^p-norm for the pixel generation has then the form

$$\ell_{\mathrm{o}}^p(\boldsymbol{x}) = \sqrt[p]{\sum_{i=1}^{4} \left| \frac{\boldsymbol{n}_i \cdot (\boldsymbol{x} - \boldsymbol{x}_0)}{\mathcal{D}_i + \Delta\mathcal{D}^{\mathrm{o}}} \right|^p}. \tag{13}$$

The constant $\Delta\mathcal{D}^{\mathrm{o}}$ is used for the scaling of length and breadth of the grains. So the ratio of length to breadth is not preserved. The shape of the overlap regions is obtained by the consideration of ℓ_{o}^p for two grains 1 and 2: $\ell_{\mathrm{o},1}^p(\boldsymbol{x}) \leq 1 \wedge \ell_{\mathrm{o},2}^p(\boldsymbol{x}) \leq 1$, which means that a certain point $\boldsymbol{x}$ belongs to both grains. An additional criterion has to be used to decide, to which grain the point $\boldsymbol{x}$ belongs. A natural choice is the usage of the smaller norm as indicator for the affiliation, where $\boldsymbol{x}$ is assumed to be a point of the grain with the smaller ℓ_{o}^p. The exponent p is used to define the angularity of the grains and with it the roundness of the overlapping region. Fig. 5 shows three cases for overlapping. The effect of overlapping and rounding off the boundary significantly depends on the exponent p.

2.5. Periodization

The periodicity of the created structures is desirable for two reasons. Firstly, for the consideration of a mechanical problem, the boundary conditions play an crucial role. Here, a well-known fact is that periodic displacement boundary conditions together with periodic structures are a prerequisite for the determination of a realistic effective material behavior, see, e.g., Suquet[19]. Secondly, the consideration of geometric properties of a periodic structure is much more straight forward than for non-periodic ensembles, where boundary effects like intersected grains are inevitable.

The periodization of the generated microstructure is obtained by the consideration of 26 periodization boxes, in which periodically shifted copies of the seeded grains are interacting. The origin $\boldsymbol{x}_0$ is shifted by a periodization vector $\Delta\boldsymbol{x}_{ijk}^{\mathrm{p}} = w(i\,\boldsymbol{e}_1 + j\,\boldsymbol{e}_2 + k\,\boldsymbol{e}_3)$ and $\boldsymbol{x}_{ijk}^{\mathrm{p}} = \boldsymbol{x}_0 + \Delta\boldsymbol{x}_{ijk}^{\mathrm{p}},\ \ ijk = -1, 0, 1$. For every

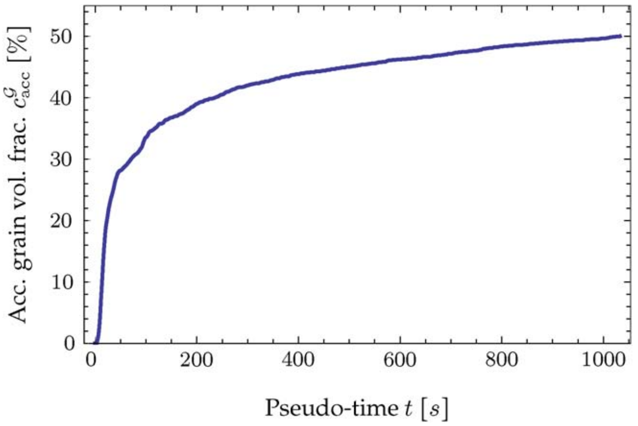

Fig. 6. Pseudo-time evolution of the accumulated volume fraction $c^{\mathcal{G}}_{\text{acc}}$ of a periodic 105 × 10 ensemble; after a steep increase in the beginning of the adsorption-and-growth process, saturation takes place, due to the steric hindrance.

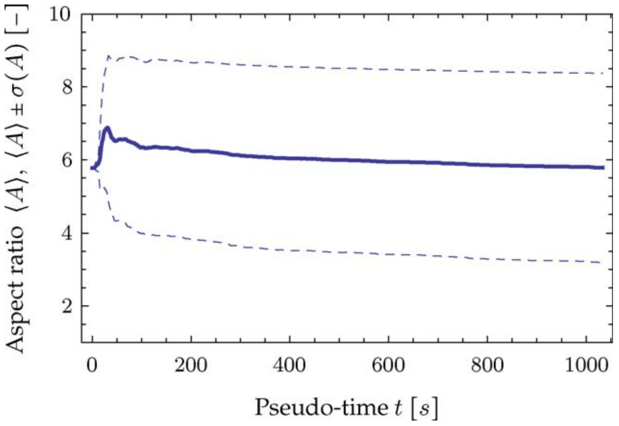

Fig. 7. Pseudo-time evolution of the mean aspect ratio $\langle A\rangle$ (—) with scatter band $\langle A\rangle \pm \sigma(A)$ (−−) for a periodic 105 × 10 ensemble; after a peak at the beginning of the structure generation process, the mean value decreases slowly, the scattering remains at a constant level.

periodic copy of a grain, the considerations in Section 2.4 have to be carried out. It is of crucial importance to keep the mean intersection points up to date. So, for every case of collision of two grain copies, the recent intersection points $\boldsymbol{p}^{\text{m},\,rec}_{ijk,n}$, $n = 1, 2$ have to be updated. All other intersection points $\boldsymbol{p}^{\text{m}}_{ijk,n}$ have to be updated as well, which is done by $\boldsymbol{p}^{\text{m}}_{ijk,n} = \boldsymbol{p}^{\text{m},\,rec}_{ijk,n} - \Delta\boldsymbol{x}^{\text{p},\,rec}_{ijk,n} + \Delta\boldsymbol{x}^{\text{p}}_{ijk}$, $n = 1, 2$, where $\Delta\boldsymbol{x}^{\text{p},\,rec}_{ijk,n}$ is the offset of the recent grain copy.

3. Numerical results of the microstructural model

3.1. Pseudo-time evolution of microstructure

The pseudo-time evolution of statistical geometric quantities will be considered in this section. The best known property of microstructures is the volume fraction of particles. As pointed out by, e.g., Becher et al.[3], the distribution of grain size and aspect ratio plays a crucial role for the fracture toughness.

Thus, Fig. 6 assembles the pseudo-time evolution of the volume fraction, the mean aspect ratio and its standard deviation. The volume of one grain is determined by $V^{\mathcal{G}} = 3/2\sqrt{3}B^2H$, so the accumulated grain volume is $V^{\mathcal{G}}_{\text{acc}} = \sum_{i=1}^{n^{\mathcal{G}}} V^{\mathcal{G}}_i$. The grain volume fraction is the ratio of the accumulated grain volume to the volume of the region of interest $c^{\mathcal{G}}_{\text{acc}} = V^{\mathcal{G}}_{\text{acc}}/w^3$. The grain volume fraction of a single grain normalized on the accumulated grain volume is $c^{\mathcal{G}} = V^{\mathcal{G}}/V^{\mathcal{G}}_{\text{acc}}$. The aspect ratio A of a grain is the ratio of length to breadth of a body. For hexagonal prisms $A = H/\sqrt{3}B$, if the width across flats is regarded as small diameter. For the determination of the mean value of A, the grain volume fraction $V^{\mathcal{G}}$ is used as basis volume, such that $\langle A\rangle = \sum_{i=1}^{n^{\mathcal{G}}} c^{\mathcal{G}}_i A_i$, where the grain volume fractions $c^{\mathcal{G}}_i$, $i = 1 \ldots n^{\mathcal{G}}$ act as weights of the sum. The standard deviation is calculated by $\sigma(A) = \sqrt{\sum_{i=1}^{n^{\mathcal{G}}} c^{\mathcal{G}}_i (A_i - \langle A\rangle)^2}$.

The following figures show the evolution of a periodic ensemble of grains in a cell of width $w = 16$ without any overlapping after case 2. It is, therefore, an exact geometric ensemble consisting of non-penetrating hexagons. It consists of 105 seed steps of each 10 grains. So a total of 27 × 105 × 10 = 28, 350 entities have to be considered in the final time step. The growth velocity parameters Eqs. (8) and (9) are $k_L = 10k_B = 10$, the penalty factors after Section 2.3 and Eq. (7) are $k^{\text{pen}} = 1/10$ and $\Delta\mathcal{D}^{\text{pen}} = 1/10$.

Fig. 6 shows the pseudo-time evolution of the grain volume fraction $c^{\mathcal{G}}$. The steep accession in the beginning is due to the free growth of the grains, mainly without steric hindrance. At a grain volume fraction of around 25%, the grain interaction gains increasing influence, which causes a certain saturation of the grain volume fraction. The final value of $c^{\mathcal{G}}$ lies at 50%, which can be considered to be a high value for a complicated randomized structure without overlapping. [12] The trend at the end of the process is already towards increasing volume fraction.

In Fig. 7, the mean aspect ratio $\langle A\rangle$ with its scatter band $\pm\sigma(A)$ is depicted. Here it can be seen that a structure with aspect ratios ≈6 with a relatively wide variance ≈2 is generated by the usage of the mentioned generator setup. The mean aspect ratio of the structure reaches a local peak at the pseudo-time, when the grains come into interaction, i.e., the pseudo-time, when saturation of the volume fraction begins. After this point in time, the aspect ratio is monotonically decreasing, because the hindrance in axial direction is more likely than in radial direction.

It is important to gain insight into the influence of the parameters for the control of the growth process. Therefore, parameter variations on the base of the already mentioned set of input values have been carried out. The following diagrams show the mean aspect ratio $\langle A\rangle$ over the grain volume fraction $c_{\mathcal{G}}$, due to their significance for the silicon nitride microstructure.

One important factor is the growth velocity parameter k_L. It has been varied, since it has a noteworthy impact on the aspect ratio of the obtained structures. In the beginning of the process, a broad distribution can be observed. The seeding penalty factor $k^{\text{pen}} = 1/2$ is chosen to enforce more space for the structure generation process with higher growth anisotropies (Section 2.3). After a peak of the aspect ratio, which is shifted to lower volume fractions for greater axial growth velocities, all curves appear converging at a mean aspect ratio of ≈6, and a volume fraction of ≈60%. Hence, a merely temporary impact on the mean value

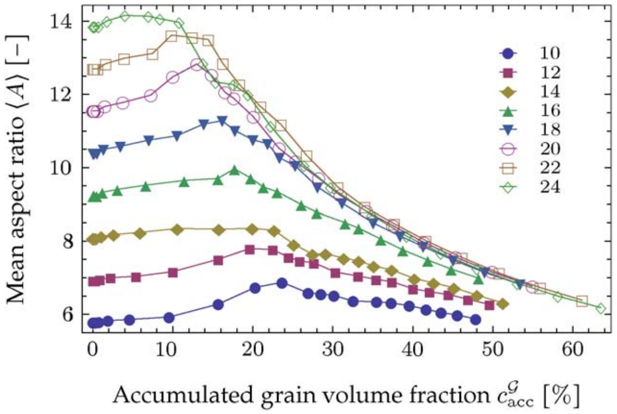

Fig. 8. Mean aspect ratio ⟨A⟩ over grain volume fraction $c^{\mathcal{G}}_{\text{acc}}$ of a periodic 105 × 10 ensemble for a variation of the ratio of the growth constants $k_L/k_B = 10 \ldots 24$ and $k_B = 1 = \text{const}.$, $k^{\text{ga}} = 9/10$, $c_{B/L} = 1/5$, $k^{\text{pen}} = 1/2$, $\Delta\mathcal{D}^{\text{pen}} = 1/10$; the impact of the axial grain growth velocity on the mean aspect ratio is significant only in the beginning of the structure generation process.

of the aspect ratio is observed by this factor. The relevance for the distribution A/L will be shown in Section 3.2.

3.2. Distribution of the geometric quantities

The statistical distribution of geometric quantities is important for a comparison of artificial microstructures with experimental data. Additionally, it is relevant to gain further insight into the behaviour of the structural model. So the example of Section 3.1, Fig. 8 is readopted. Fig. 9 depicts probability densities of the aspect ratio and the grain length for different grain growth anisotropies. The probability density is the grain volume fraction normalized on the total grain volume. In order to adjust the grain volume fraction to from ≈60% to the natural fraction of 88%, an overlapping factor of $\Delta\mathcal{D}^{\text{o}} = 0.262$ has been chosen, see Eq. (13) and Fig. 5. Natural slightly rounded grain edges have been obtained by a norm exponent $p = 20$.

So, the influence of the growth velocity anisotropy can, now, be seen in detail. Although similar mean aspect ratios (and grain lengths) are observed in the pseudo-time evolution in Fig. 8, the distribution is obviously different. A trend for higher aspect ratios and longer grains with leaner scattering is observed for increasing growth anisotropy. The experimental reference data has been acquired from SEM micrographs of the commercial silicon nitride grade SL 200 BG by an elaborated digital image processing technique.[13] The main problem in measuring structural data of complex microstructures is the fact that an elongated grain can be intersected in many different ways, see, e.g., Ohser und Mücklich.[20] A rational estimation of the grain length and aspect ratio is, therefore, in general a contingency. Fig. 10 shows the problem: the grain is intersected by three different planes. The brown plane (●) contains the grain axis. Hence, the grain's length and aspect ratio is represented realistically. Differently the green plane (●): here, the whole cross section is intersected, but in a skew angle. So the grain appears much smaller and with significantly decreased aspect ratio, than it has in reality. The limiting case would be a section plane, which is perpendicular to the grain axis. Here, any information on grain length and aspect ratio would be lost. A further undesirable but also inevitable case is represented by the blue plane (●), which is sectioning only a small part of the whole cross section. The result is an irregular polygon, which does not even allow for a serious prediction of the grain thickness.

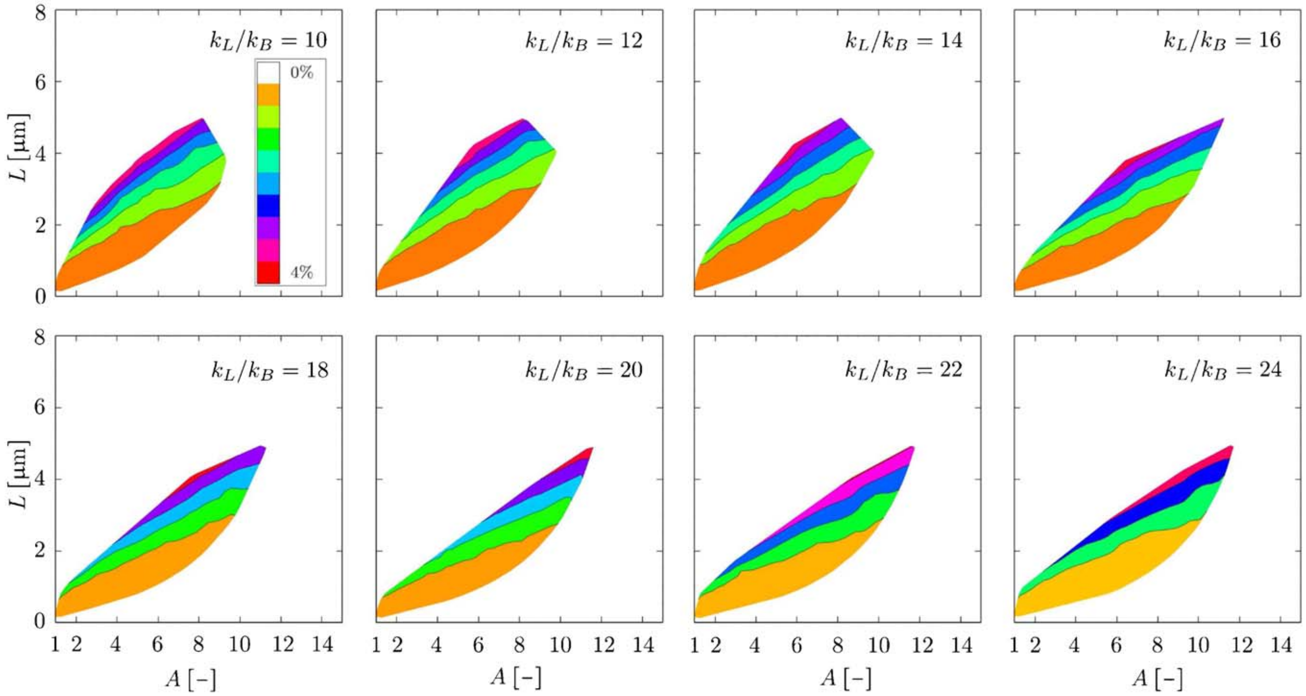

Fig. 9. Cumulative frequency of aspect ratios periodic 105 × 10 ensembles for the parameter setup $k_L/k_B = 10 \ldots 24$, $k^{\text{ga}} = 9/10$, $c_{B/L} = 1/5$, $k^{\text{pen}} = 1/2$, $\Delta\mathcal{D}^{\text{pen}} = 1/10$, $\Delta\mathcal{D}^{\text{o}} = 0.262$ and $p = 20$.

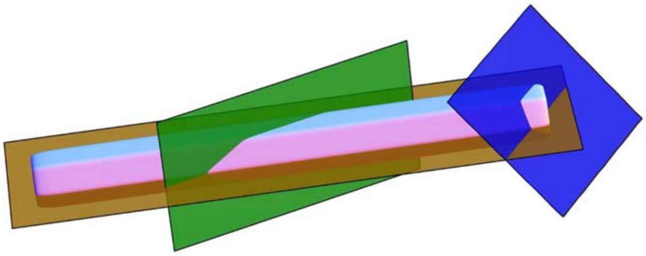

Fig. 10. Grain with different section planes: axis parallel section (●) delivers original representation of the grain shape; section through the grain axis (●) yields a smaller section and, therefore, an underestimation of the aspect ratio; shape of the edge section (●) delivers completely unrealistic information about the grain shape. (For interpretation of the references to color in this figure legend, the reader is referred to the web version of the article.)

A well established procedure is the transformation of measurable two-dimensional distributions of size and shape into distributions of spatial size and shape. Mücklich et al.[21] applied this technique first to the demanding case of silicon nitride. The idea is that a planar section through a spatial distribution of (non-overlapping) hexagonal prisms will result in a distribution of convex intersection polygons. So a stereological function in form of a linear map can be formulated as link between planar and spatial distribution of size and shape quantities. The kernel of this function for complicated shapes like hexagonal prisms can only be calculated in a discretized way due to the huge amount of intersection possibilities (Fig. 10). In this line, simulations with randomly intersected hexagonal prisms have been carried out in order to acquire the coefficients of the kernel function. The relative frequencies of the spatial quantities then can be calculated by the EM algorithm, see Vardi et al.,[22] which was introduced into stereology by Silvermann et al.[23]

Fünfschilling et al.[13] measured the microstructural properties of the commercial silicon nitride grade SL 200 BG with the image processing software ImageC (Aquinto, Berlin, Germany) and the stereology extension based on the work of Mücklich et al.[21] For the measurement, an ensemble of approximately 3000 grains has been examined.

The generated microstructure is determined by the grain growth velocity parameter combination $k_L/k_B = 22$. The other parameters are as described in Section 3.1 and in Figs. 8 and 9.

Fig. 11 juxtaposes a SEM micrograph of SL 200 BG and a two-dimensional section through the artificial three-dimensional structure with the mentioned parameters. In both cases, large and elongated as well as smaller and more roundish grains can be seen. A certain similarity between the two structures cannot be neglected. Therefore, a view to the most important geometrical properties of grain length and aspect ratio delivers further insight. Fig. 12 shows two diagrams with the probability density as function of aspect ratio and grain length. For SL 200 BG, the probability density is calculated after,[21] as described before. The diagram for the generated structure uses the grain volume fraction of the single grains in the three-dimensional structure as probability density. The two diagrams show certain differences: the SL 200 BG plot has several peaks. Two main peaks are clearly recognizable. The first one is at small grain lengths beneath 1 μm and has local peaks at aspect ratios between 2 and 4. These peaks represent grain shape/grain length combinations with minor relevance for the fracture toughness of the material, because the grains are too small to bear the high local loads around crack tips.[2,3] The other peak is at high grain lengths of 4 μm and high aspect ratios of ≈10. This peak has a close relationship for the high fracture toughness of this material, because it means that the material contains a significant amount of strong and elongated grains, which can act as bridging grains and, therefore, avoid quick crack propagation.[13] Interesting is the observation that a region between those peaks exists, in which hardly any grain can be found.

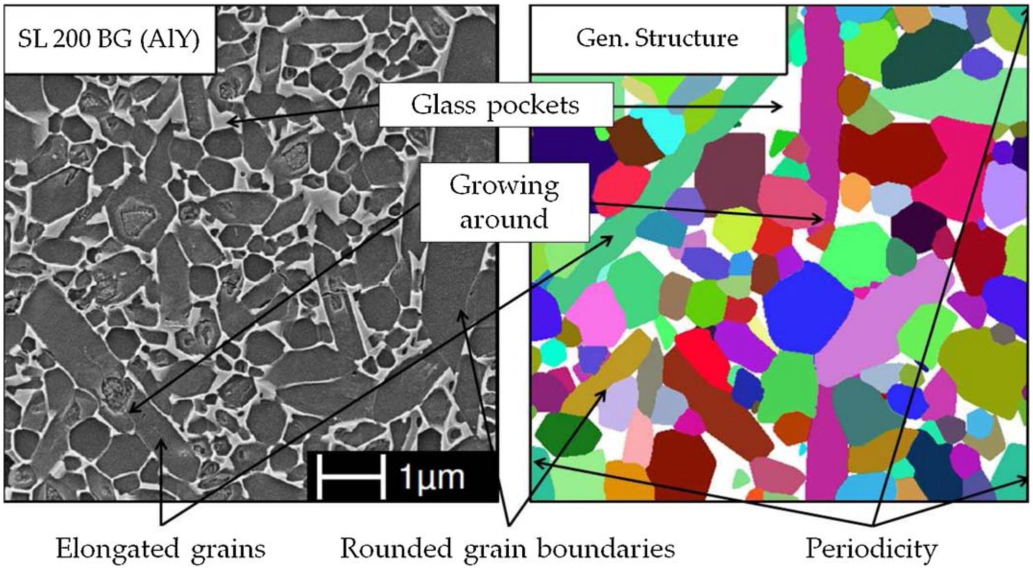

Fig. 11. SEM-image of the AlY-doped commercial silicon nitride grade SL 200 BG[13] and an exemplary section image of the generated periodic three-dimensional microstructure with 105×10 grains and the parameters $k_L/k_B = 22$, $k^{\mathrm{ga}} = 9/10$, $c_{B/L} = 1/5$, $k^{\mathrm{pen}} = 1/2$, $\Delta\mathcal{D}^{\mathrm{pen}} = 1/10$, $\Delta\mathcal{D}^{\mathrm{o}} = 0.262$ and $p = 20$. The most important features of the silicon nitride structure can be identified clearly.

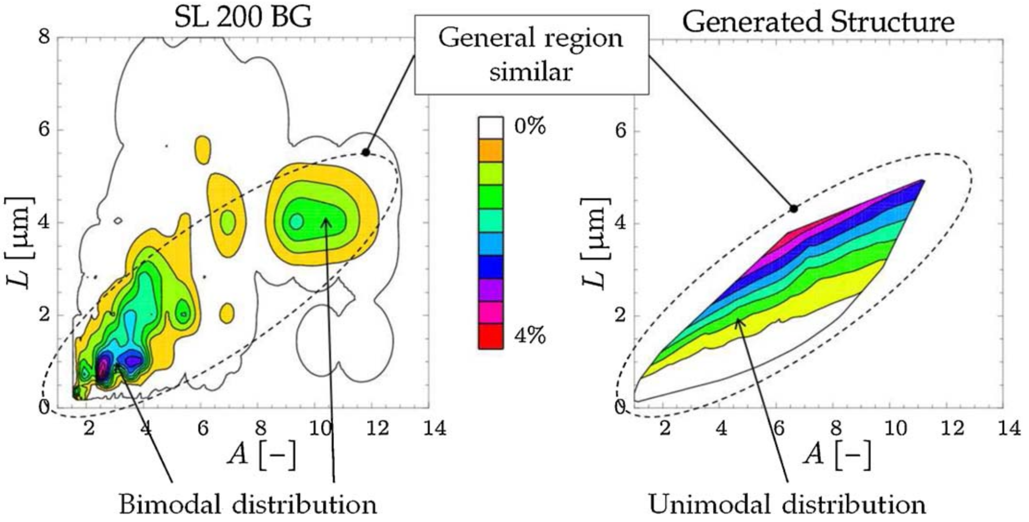

Fig. 12. Cumulative frequency of aspect ratios in SL 200 BG[13] and in a periodic 105 × 10 ensemble for $k_L/k_B = 22$, $k^{\text{ga}} = 9/10$, $c_{B/L} = 1/5$, $k^{\text{pen}} = 1/2$, $\Delta\mathcal{D}^{\text{pen}} = 1/10$, $\Delta\mathcal{D}^{\text{o}} = 0.262$ and $p = 20$. The distributions of the experimental data and the generated structure are mainly in the same region, however, the bimodality of the data is not captured by the simulation.

The diagram for the generated microstructure covers a similar domain, although it shows differences as well. The distribution does not show strongly pronounced peaks and its global maximum is not at the same position as in the stereological observation. Nevertheless, the main trend is towards long and elongated grains, which appear at similar grain lengths and aspect ratios. Reasons for the differences between the two diagrams can be attributed firstly to a simplification of the structure evolution in the presented algorithm and secondly to the differences with respect to the acquisition of the underlying data. The comparison of the results from the thermodynamical simulations of Kitayama et al.[6] with the data, which was gained from the structure generation process shows good agreement, as well. Although, it has to be mentioned that the distributions of grain length over grain width and aspect ratio over grain width from the presented algorithm are broader with the chosen parameter combinations.

4. Finite element simulations

4.1. Discretized geometry

The finite element model is based on a periodic ensemble of 232 grains. The structure was created by the described seed-and-growth algorithm with 29 seed steps per 8 grains. It has a grain volume fraction of 88%, a mean aspect ratio of 5.2 and a mean grain length of 7.6 μm. Fig. 13a is a three-dimensional contour plot of a high fidelity discretization (200^3 voxel). The geometric features like hexagonal and elongated or roundish grains and the periodicity of the structure can be seen well. Fig. 13b shows the corresponding finite element mesh, generated by the meshing tool ScanIP by Simpleware.[15] Grains are pictured as coloured grains. Significantly elongated grains besides roundish or intersected ones can be recognized. The gray regions represent the glass matrix, which fills 12 vol.%. The structural model preserves the exact periodicity of the generated structure, but slight deviations can be observed as well. Due to the great flexibility of the meshing algorithm, a certain lack of fidelity has to be tolerated. The model contains over 450,000 degrees of freedom and over 825,000 tetrahedral elements with linear integration (C3D4).

4.2. Elastic material model

The elastic material behavior of silicon nitride on the microlevel obeys Hooke's law

$$\boldsymbol{\sigma} = \mathbb{C}(\boldsymbol{x})[\boldsymbol{\varepsilon}], \tag{14}$$

where the stiffness tensor $\mathbb{C}(\boldsymbol{x})$ depends on the considered material point, i.e., the grain. The glassy matrix phase ($\mathcal{M}$) is assumed to be an isotropic elastic aggregate, such that the elastic stiffness tensor $\mathbb{C}^{\mathcal{M}}$ is determined by the two eigenvalues $3K^{\mathcal{M}}$ and $2G^{\mathcal{M}}$

$$\mathbb{C}^{\mathcal{M}} = 3K^{\mathcal{M}}\mathbb{P}_1 + 2G^{\mathcal{M}}\mathbb{P}_2, \tag{15}$$

with the bulk modulus $K^{\mathcal{M}}$ and the shear modulus $G^{\mathcal{M}}$, which are connected to the volumetric and deviatoric projectors $\mathbb{P}_1 = 1/3\,\boldsymbol{I} \otimes \boldsymbol{I}$ and $\mathbb{P}_2 = \mathbb{I}^S - \mathbb{P}_1$, respectively. The relations

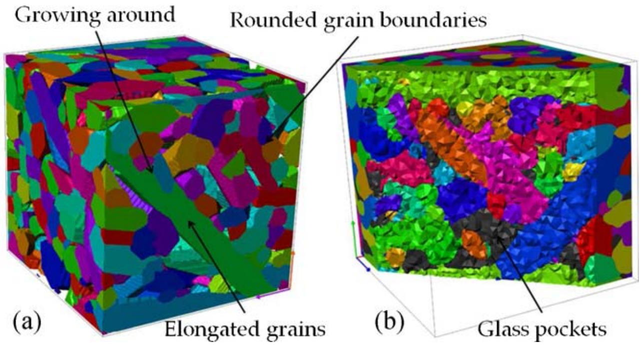

Fig. 13. Periodic 232 grain ensemble: (a) high fidelity surface mesh and (b) used finite element mesh; the arrows indicate the important features of silicon nitride.

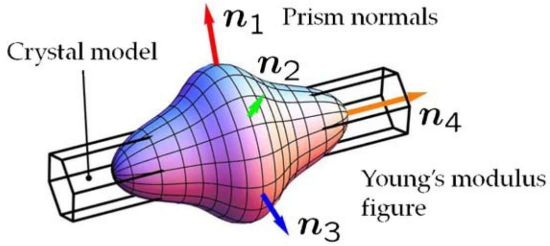

Fig. 14. Hexagonal prism as grain model together with the spherical projection of the grains stiffness tensor $\mathbb{C}^{\mathcal{G}}$ and prism normal vectors $\boldsymbol{n}_i$, $i = 1 \ldots 4$.

between the eigenvalues and the engineering constants Young's modulus $E^{\mathcal{M}}$ and Poisson's ratio $\nu^{\mathcal{M}}$ are

$$K^{\mathcal{M}} = \frac{E^{\mathcal{M}}}{3(1-2\nu^{\mathcal{M}})} \quad \text{and} \quad G^{\mathcal{M}} = \frac{E^{\mathcal{M}}}{2(1+\nu^{\mathcal{M}})}. \tag{16}$$

The matrix material is mostly an oxynitride glass, thus the constants are assumed to be $E^{\mathcal{M}} = 133\,\text{GPa}$ and $\nu^{\mathcal{M}} = 0.29$, see Hampshire et al.[24]

The hexagonal grains ($\mathcal{G}$) are elastic transverse-isotropic. Therefore, five linear independent elastic constants can be measured, if hyperelasticity is assumed. In general the elastic stiffness tensor can be denoted by

$$\mathbb{C}^{\mathcal{G}} = C^{\mathcal{G}}_{\alpha\beta}\, \boldsymbol{B}_\alpha \otimes \boldsymbol{B}_\beta. \tag{17}$$

The elastic constants are provided in Vogelgesang et al.[25] and have the values $C^{\mathcal{G}}_{11} = 433\,\text{GPa}$, $C^{\mathcal{G}}_{33} = 574\,\text{GPa}$, $C^{\mathcal{G}}_{12} = 195\,\text{GPa}$, $C^{\mathcal{G}}_{13} = C^{\mathcal{G}}_{23} = 127\,\text{GPa}$, $C^{\mathcal{G}}_{44} = 119\,\text{GPa}$ and $C^{\mathcal{G}}_{66} = 108\,\text{GPa}$. Additionally, the relation $C^{\mathcal{G}}_{12} = 1/2\,(C^{\mathcal{G}}_{11} - C^{\mathcal{G}}_{44})$ holds. All other components are zero in the principal orientation. The symmetric orthonormal basis tensors of 2nd-order $\boldsymbol{B}_\alpha$ are given by $\boldsymbol{B}_1 = \boldsymbol{e}_1 \otimes \boldsymbol{e}_1$, $\boldsymbol{B}_2 = \boldsymbol{e}_2 \otimes \boldsymbol{e}_2$, $\boldsymbol{B}_3 = \boldsymbol{e}_3 \otimes \boldsymbol{e}_3$, $\boldsymbol{B}_4 = \sqrt{2}\ \mathrm{sym}(\boldsymbol{e}_1 \otimes \boldsymbol{e}_2)$, $\boldsymbol{B}_5 = \sqrt{2}\ \mathrm{sym}(\boldsymbol{e}_3 \otimes \boldsymbol{e}_1)$, $\boldsymbol{B}_6 = \sqrt{2}\ \mathrm{sym}(\boldsymbol{e}_2 \otimes \boldsymbol{e}_3)$, according to Federov[26] with the symmetry operator $\mathrm{sym}(\boldsymbol{A}) = 1/2(\boldsymbol{A} + \boldsymbol{A}^\top)$. Note, that the basis tensors of the shear planes have a prefactor of $\sqrt{2}$ due to the normalized Voigt convention, which allows for a simple implementation of the orientation transformation. The orientation of the elastic stiffness is determined grainwise by three angles (Section 2.2) from the structure generation process, and is applied on the basis tensors $\boldsymbol{B}_\alpha$ by an active transformation. Fig. 14 shows a crystal model together with its normal vectors and the spherical projection of the grain stiffness tensor $\mathbb{C}^{\mathcal{G}}$ according to Böhlke and Brüggemann.[27] The grains exhibit a significantly pronounced tensile stiffness in the grain axis direction.

4.3. Projected periodic boundary conditions

Periodic displacement boundary conditions are a well-established way for solving problems in solid mechanics, which have to remain uninfluenced by boundary effects. The displacement field on a boundary of a continuum problem can be described by the relation $\boldsymbol{u}^\pm = \bar{\boldsymbol{\varepsilon}}\boldsymbol{x}^\pm + \boldsymbol{w}^\pm$, where $\boldsymbol{u}^\pm$ are the total displacements on a positive (+) or negative (−) boundary of a periodic ensemble, undergoing an effective strain $\bar{\boldsymbol{\varepsilon}}$. The displacement fluctuations $\boldsymbol{w}^\pm$ on opposing sides are assumed to be equal for every material point on the boundary in a non-trivial way for a heterogeneous medium, which is expressed by the periodicity condition $\boldsymbol{w}^+ = \boldsymbol{w}^-$. This yields the constraint equation for the boundary displacements $\boldsymbol{u}^+ - \boldsymbol{u}^- = \bar{\boldsymbol{\varepsilon}}(\boldsymbol{x}^+ - \boldsymbol{x}^-)$. For finite element simulations, a weaker approach has to be chosen, due to the discretization of the geometry. The best way is the usage of a mesh with corresponding nodes on the opposing sides. This is of course a significant challenge, because even for perfectly periodic structures, the periodicity of the discretization has to be enforced for its own. Fritzen and Böhlke[28] have implemented this for periodic three-dimensional Voronoï tessellations by extending an existing mesh generator. For commercial meshing tools, such demanding implementation is mostly not possible. A feasible way is the implementation of projected boundary conditions, where the nodes from one side are projected on mesh triangles of the other side. The displacements to the projected node are obtained by a linear interpolation with the triangle nodes. Details of the implementation can be found in Ref.[14]

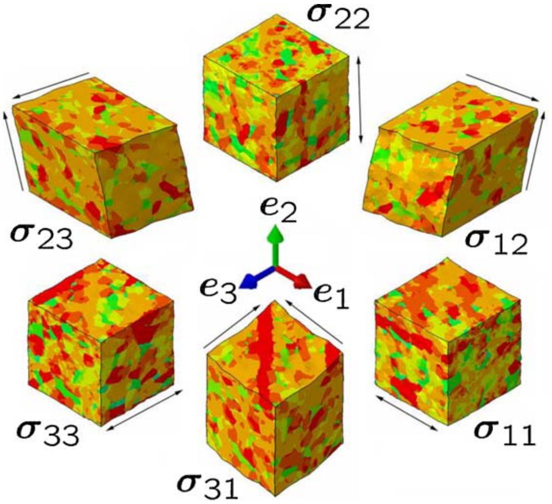

Fig. 15. Six deformation modes on a periodic unit cell with 232 grains. The arrows indicate the deformation directions. The plotted fields represent the stress distributions, which is inhomogeneous but periodic.

4.4. Elastic homogenization

For the homogenization of elastic properties, several types of methods such as estimates and bounds exist see, e.g., Ponte Castañeda and Suquet,[29] Böhlke et al.[30] or Drach et al.[31] In the context of a finite element based approach, the homogenization of heterogeneous elastic aggregates can be carried out by the consideration of the ensemble averages of the stress tensors $\langle \boldsymbol{\sigma}_\alpha \rangle$. To obtain the 21 components of the homogenized stiffness tensor, six orthogonal effective deformation modes $\bar{\boldsymbol{\varepsilon}}_\beta = \bar{\varepsilon}_0 \boldsymbol{B}_\beta$ with corresponding periodic displacement fluctuations (Fig. 15) are prescribed, such that the stiffness components can be obtained by $\overline{C}_{\alpha\beta} = \langle \boldsymbol{\sigma}_\alpha \rangle \cdot \boldsymbol{B}_\beta / \bar{\varepsilon}_0$. Due to the elastic isotropy of bulk silicon nitride, the consideration of the isotropic parts of the obtained effective stiffness delivers effective values for the engineering constants. This is obtained by the isotropic projections of the volumetric and deviatoric part of $\overline{\mathbb{C}}$. The effective bulk modulus is determined by $3\overline{K} = \overline{\mathbb{C}} \cdot \mathbb{P}_1/\|\mathbb{P}_1\|$, and the effective shear modulus is given by $2\overline{G} = \overline{\mathbb{C}} \cdot \mathbb{P}_2/\|\mathbb{P}_2\|$. Therefore, the effective engineering constants Young's modulus $\overline{E} = 302$ GPa and Poisson's ratio $\overline{\nu} = 0.28$ are calculated following Eq. (16). The maximum deviation from isotropy is 5%, such that the values are in good correspondence with literature values, see, e.g., Roebben et al.[32] or Lube and Dusza.[33]

5. Summary

A simplified algorithm for the generation of periodic three-dimensional silicon nitride-like structures has been introduced. Its primal result is the creation of microstructural models for micromechanical finite element simulations. The microstructure generator is based on a sequential adsorption procedure, which is enriched with growth of particles, steric hindrance and overlapping, motivated by experimental observations of Krämer et al.[34] These observations have been implemented in algorithmic detail to preserve high aspect ratios and grain volume fractions in the artificial microstructures.

In order to give an insight into the behavior of the model, the pseudo-time evolution of mean aspect ratio and grain volume fraction have been discussed for different parameter sets of a periodic ensemble of 1050 grains, which have been adsorped in 105 steps. It was shown that the mean aspect ratio in generated microstructures decreases after a temporary peak at approximately 20% grain volume fraction due to steric hindrance.

The impact of the axial growth rate on the pseudo-time evolution and the distribution of the geometric quantities aspect ratio and grain length has been examined. The pseudo-time evolution showed a certain convergence of aspect ratios at values of approximately 6 and volume fractions ratios of approximately 60%, which could be obtained without overlapping. Realistic grain volume fractions have been adjusted by variation of the grain overlapping. The adjusted ensembles have been considered with respect to the probability density of the aspect ratio and grain length. A clear redistribution of the densities to longer grains and with higher aspect ratios was caused by increased grain growth anisotropy.

The significance of the model has been shown by a comparison of the grain length and the aspect ratio distribution with literature values,[13] showing reasonable correspondence. Hereby, a general accordance of the stereological SEM image evaluation with the data provided by the structure generator was observed. However, differences have been observed as well, concerning the bimodality of the probability density of grain length and aspect ratio. On the one hand, these can be attributed to the assumptions which have been made for the implementation of the structural model. On the other hand, the procedures of the acquisition of the distributions for the SEM images and for the data from the structure generator is different, which should induce, as well, differences in the obtained distributions.

Aside from these issues, the structure generator reproduced the main features of a real silicon nitride microstructure, which has been shown by a comparison of a SEM micrograph of SL 200 BG and a synthetic microstructure.

The major relevance of the structural model is the application as geometric information for micromechanical finite element simulations, which have been carried out in an elastic anisotropic framework. In order to determine the effective elastic constants, six periodic deformation modes on a periodic unit cell with 232 grains under projected boundary conditions have been carried out and used for the homogenization. The well-known effective values for Young's modulus and Poisson's ratio of bulk silicon nitride have been reproduced by this technique.

6. Conclusions

Based on the aforementioned results, it can be concluded that the algorithmic structural model is generally capable of the generation of realistic silicon nitride microstructures. Considering all discussed features, we conclude that the model appears as a reasonable approximation for the complex reality of the silicon nitride structure. Thus, it can be used for the numerical considerations of more complicated material behavior like thermoelasticity with trans- and intergranular fracture, which will be presented in a forthcoming paper.

The general technique of sequential adsorption with growth and steric hinderance of particles is applicable to many different types of materials.

Acknowledgement

This work was funded by the German Research Foundation (DFG) within the Center of Excellence SFB 483 in the subprojects C8 (Mechanism-based micromechanical simulation of crack propagation in in-situ-reinforced high performance ceramics).

References

1. Lange F. Relation between strength, fracture energy, and microstructure of hot-pressed Si_3N_4. *J Am Ceram Soc* 1973;**56**:518–22.
2. Ohji T, Hirao K, Kanzaki S. Fracture resistance behavior of highly anisotropic silicon nitride. *J Am Ceram Soc* 1995;**78**:3125–8.
3. Becher PF, Sun EY, Plucknett KP, Alexander KB, Hsueh CH, Lin H-T, Waters SB, Westmoreland C-G. Microstructural design of silicon nitride with improved fracture toughness I: Effects of grain shape and size. *J Cryst Growth* 1998;**81**:2821–30.
4. Peillon FC, Thevenot F. Microstructural designing of silicon nitride related to toughness. *J Eur Ceram Soc* 2002;**22**:271–8.
5. Sun EY, Becher PF, Plucknett KP, Hsueh C-H, Alexander KB, Waters SB. Microstructural design of silicon nitride with improved fracture toughness II: Effects of yttria and alumina additives. *J Am Ceram Soc* 1998;**81**:2831–40.
6. Kitayama M, Hiraro K, Toriyama K, Kanzaki S. Modeling and simulation of grain growth in Si_3N_4—I. *Anisotropic Ostwald ripening Acta Metall* 1998;**46**(18):6541–50.
7. Kitayama M, Hiraro K, Toriyama M, Kanzaki S. Modeling and simulation of grain growth in Si_3N_4—II. The α-β transformation. *Acta Metall* 1998;**46**(18):6551–7.
8. Kitayama M, Hiraro K, Toriyama M, Kanzaki S. Modeling and simulation of grain growth in Si_3N_4—III. Tip shape evolution. *Acta Mater* 2000;**48**:4635–40.

9. Borbély A, Kenesei P, Biermann H. Estimation of the effective properties of particle-reinforced metal-matrix composites from microtomographic reconstructions. *Acta Mater* 2006;**54**:2735–44.
10. Louis P, Gokhale A. Computer simulations of spatial arrangement and connectivity of particles in three-dimensional microstructure: application to model electrical conductivity of polymer matrix composites. *Acta Mater* 1996;**44**:1519–28.
11. Tschopp MA, Wilks GB, Spowart JE. Multi-scale characterization of orthotropic microstructures. *Mod Sim Mat Sc Eng* 2008;**16**:1–14.
12. Cooper DW. Random-sequential-packing simulations in three dimensions for spheres. *Phys Rev A: At Mol Opt Phys* 1988;**38**:522–4.
13. Fünfschilling S, Fett T, Hoffmann MJ, Oberacker R, Schwind T, Wippler J, et al. Mechanisms of toughening in silicon nitrides: the roles of crack bridging and microstructure. *Acta Mater* 2011;**59**:3978–89.
14. Wippler J, Fünfschilling S, Fritzen F, Böhlke B, Hoffmann MJ. Homogenization of the thermoelastic properties of silicon nitride. *Acta Mater* 2011;**59**:6029–38.
15. Young PG, Beresford-West TBH, Coward SRL, Notarberardino B, Walker B, Abdul-Aziz A. An efficient approach to converting three-dimensional image data into highly accurate computational models. *Philos Trans R Soc Lond Ser A* 2008;**366**:3155–73.
16. Shoemake K. Uniform random rotations. In: Kirk D, editor. *Graphics Gems III*. London: Academic Press Inc; 1992. p. 124–32.
17. Ahrens JH, Kohrt KD. ALGORITHM 599—sampling from Gamma and Poisson distributions. *ACM Trans Math Softw* 1983;**9**(2):255–7.
18. Krämer K, Hoffmann MJ, Petzow G. Grain growth kinetics of Si_3N_4 during α/β-transformation. *Acta Metall* 1993;**41**(10):2939–47.
19. Suquet PM. Plasticité et homogénéisation. PhD thesis, Université Pierre et Marie Curie, Paris, 1982.
20. Ohser J, Mücklich F. *Statistical analysis of microstructures in materials science*. Hoboken: Wiley-VHC; 2000.
21. Mücklich F, Hartmann S, Hoffmann MJ, Schneider GA, Ohser J, Petzow G. Quantitative description of Si_3N_4 microstructures. *Key Eng Mater* 1994;**5**:465–70.
22. Vardi Y, Shepp LA, Kaufman L. A statistical model for positron emission tomography. *J Am Stat Soc* 1985;**80**(389):8–37.
23. Silverman BW, Jones MC, Wilson JD, Nychka DW. A smoothed EM approach to a class of problems in image analysis and integral equations. *J R Stat Soc B* 1990;**52**:271–324.
24. Hampshire S, Nestor E, Flynn R, Goursat P, Sebai M, Thompson DP, et al. Yttrium oxynitride glasses: properties and potential for crystallisation to glass–ceramics. *J Eur Ceram Soc* 1994;**14**:261–73.
25. Vogelgesang R, Grimsditch M, Wallace JS. The elastic constants of single crystal β-Si_3N_4. *Appl Phys Lett* 2000;**76**(8):982–4.
26. Federov F. *Theory of elastic waves in crystals*. New York: Plenum Press; 1968.
27. Böhlke T, Brüggemann C. Graphical representation of the generalized Hooke's law. *Techn Mech* 2001;**21**(2):145–58, http://preview.tinyurl.com/6e9uxkc.
28. Fritzen F, Böhlke T. Periodic three-dimensional mesh generation for particle reinforced composites with application to metal matrix composites. *Int J Solids Struct* 2010;**48**(5):706–18.
29. Ponte Castañeda P, Suquet P. Nonlinear composites. *Adv Appl Mech* 1998;**34**:171–302.
30. Böhlke T, Jöchen K, Kraft O, Löhe D, Schulze V. Elastic properties of polycrystalline microcomponents. *Mech Mater* 2010;**42**:11–23.
31. Drach B, Tsukrov I, Gross T, Dietrich S, Weidenmann S, Piat R, Böhlke T. Numerical modeling of carbon/carbon composites with nanotextured matrix and 3D pores of irregular shapes. *Int J Solids Struct* 2011, doi:10.1016/j.ijsolstr.2011.04.021.
32. Roebben G, Erauw J-P, Lube T, Duan RG, Cambier F, Van der Biest O. Microstructure characteristics related to the high temperature fracture resistance of the ESIS silicon nitride reference material. In: Neimitz A, Rokach IV, Kocanada D, Golos K, editors. *Fracture Mechanics Beyond 2000 - Proc of ECF 14, vol. III*. Sheffield: EMAS Publications; 2002. p. 77–84.
33. Lube T, Dusza J. A silicon nitride reference material - a testing program of ESIS TC6. *J Eur Ceram Soc* 2007;**27**:1203–9.
34. Krämer M, Wittnüss D, Küppers H, Hoffmann MJ, Petzow G. Relations between crystal structure and growth morphology of β-Si_3N_4. *J Cryst Growth* 1994;**140**:157–66.